

Near-infrared spectroscopy of embedded protostars in the massive metal-poor star forming region NGC 346

O. C. Jones¹★, M. Reiter^{1,2}, R. Sanchez-Janssen¹, C. J. Evans^{1,3}, C. S. Robertson⁴,
M. Meixner⁵ and B. Ochsendorf⁶

¹UK Astronomy Technology Centre, Royal Observatory, Blackford Hill, Edinburgh, EH9 3HJ, UK

²European Southern Observatory, Karl-Schwarzschild-Strasse 2, D-85748 Garching bei München, Germany

³European Space Agency (ESA), ESA Office, Space Telescope Science Institute, 3700 San Martin Drive, Baltimore, MD 21218, USA

⁴Institute for Astronomy, University of Edinburgh, Blackford Hill, Edinburgh EH9 3HJ, UK

⁵SOFIA-USRA, NASA Ames Research Center, MS 232-12, Moffett Field, CA 94035, USA

⁶Department of Physics and Astronomy, Johns Hopkins University, 3400 North Charles Street, Baltimore, MD 21218, USA

Accepted XXX. Received YYY; in original form 2 September 2022

ABSTRACT

We present medium-resolution ($R \sim 4000$) YJ, H & K band spectroscopy of candidate young stellar objects (YSOs) in NGC 346, the most active star-formation region in the metal-poor ($Z = 1/5 Z_{\odot}$) Small Magellanic Cloud. The spectra were obtained with the KMOS (K-Band Multi Object Spectrograph) integral field instrument on the Very Large Telescope. From our initial sample of 18 candidate high-mass YSOs previously identified from mid-IR photometry and radiative transfer model fits to their spectral energy distributions, approximately half were resolved into multiple components by our integral-field data. In total we detect 30 continuum sources and extract reliable spectra for 12 of these objects. The spectra show various features including hydrogen recombination lines, and lines from H_2 , He I and [Fe II], which are indicative of accretion, discs and outflowing material in massive YSOs. We spectroscopically confirm the youthful nature of nine YSO candidates, and identify two others as OB stars. All of the confirmed YSOs have Br γ in emission, but no emission is seen from the CO bandhead, despite other disc tracers present in the spectra. He I 1.083 μm emission is also detected at appreciably higher rates than for the Galaxy.

Key words: stars: formation – Magellanic Clouds – stars: protostars – circumstellar matter – infrared: stars.

1 INTRODUCTION

The Small Magellanic Cloud (SMC), at a distance of ~ 62 kpc (de Grijs & Bono 2015) and with a metallicity of $\sim 1/5$ solar (Peimbert et al. 2000), is actively forming stars at a rate of $\sim 0.05 M_{\odot} \text{ yr}^{-1}$ (Wilke et al. 2004). Its interstellar medium (ISM) differs significantly from that of the Milky Way, with a lower dust abundance and extreme UV extinction curve variations (which has a steep UV rise and no 2175 Å bump in the Bar; Gordon et al. 2003), providing a local proxy for a starburst galaxy reminiscent of the early universe (Dimaratos et al. 2015). Its most active (and brightest) star-forming region, NGC 346 (also known as N66, or DEM 103; Henize 1956), is located at the northern end of the SMC bar. Its H α luminosity is 60 times brighter than Orion (Kennicutt 1984) and over the last 100 Myr it is forming stars at a rate of $1.4 \times 10^{-8} M_{\odot} \text{ yr}^{-1} \text{ pc}^{-2}$ (Cignoni et al. 2011). This giant H II region is young (~ 3 Myr; Bouret et al. 2003), containing over 30 O-type stars (more than half of those known in the entire SMC; Massey et al. 1989; Evans et al.

2006) with masses in the range of 35–100 M_{\odot} (e.g., Dufton et al. 2019). *Hubble Space Telescope* (HST) imaging revealed thousands of candidate low-mass (0.6–3 M_{\odot}), pre-main-sequence (PMS) stars distributed amidst the young stars of NGC 346, and scores of small compact clusters connected by gas and dust filaments (Nota et al. 2006; Sabbi et al. 2007; Hennekemper et al. 2008; De Marchi et al. 2011). Combined, this high-resolution, multi-wavelength imaging indicates that NGC 346 has experienced an intriguing series of (presumed) sequential star-formation episodes, with the region shaped by feedback from its most massive stars.

NGC 346 has been studied extensively with *Spitzer* and *Herschel* (Simon et al. 2007; Sewilo et al. 2013; Seale et al. 2014; Ruffle et al. 2015), to identify metal-poor, young stellar objects (YSOs) in the very early stage of formation, resulting in the discovery of approximately 100 stage I, II, and III YSO candidates. Forming within the past ~ 1 Myr, these infrared-bright, candidate embedded YSOs in NGC 346 are thought to have stellar masses ranging from 1.5–17 M_{\odot} (Simon et al. 2007); most are associated with H α emission with diverse morphologies and many are found at the tip of, or inside, dusty pillars (Sewilo et al. 2013). These observations sug-

★ E-mail: olivia.jones@stfc.ac.uk

gest star formation is ongoing throughout the complex at a rate of $> 3.2 \times 10^{-3} \text{ M}_{\odot} \text{ yr}^{-1}$ (Simon et al. 2007).

Spectroscopic confirmation of massive YSOs in the SMC is currently limited to a few tens of sources (Oliveira et al. 2011, 2013, 2019; Ruffle et al. 2015; Ward et al. 2017; Rubio et al. 2018; Reiter et al. 2019). Of these, seven are located in NGC 346 (Ruffle et al. 2015; Rubio et al. 2018), with six confirmed as YSOs based on the properties of their *Spitzer* InfraRed Spectrograph (IRS) spectra. Near-IR spectroscopy is currently only available for three massive YSOs in NGC 346 (Rubio et al. 2018).

Near-IR integral-field spectroscopy of candidate YSOs in the SMC revealed a wide range of morphological and spectral properties, with seven sources exhibiting extended H_2 emission indicative of outflows in early-stage YSOs (Ward et al. 2017). In this wavelength regime, massive YSOs can be conclusively identified due to the wealth of atomic and molecular emission lines in their near-IR spectra. Ionized atomic emission lines measure the excitation of the YSO and surrounding ISM, while key features trace accretion in the inner disc region (e.g., $\text{Br}\gamma$), the presence of outflows (e.g., H_2 and $[\text{FeII}]$) and circumstellar discs (via the CO bandhead emission and fluorescent Fe II).

Medium resolution, near-IR spectroscopy of candidate YSOs in the Clouds has been conducted by Ward et al. (2016, 2017), Rubio et al. (2018), Reiter et al. (2019), van Gelder et al. (2020) and Sewilo et al. (2022). In these samples the $\text{Br}\gamma$ line has been detected at a high rate, but no conclusive relation has been found between $\text{Br}\gamma$ luminosity and metallicity, although Ward et al. (2017) suggested their YSO sample shows tentative evidence of increased accretion rates in the SMC compared to the Milky Way.

In this paper we examine the fundamental properties of massive star formation at sub-solar metallicity in NGC 346 and explore variations within the Magellanic Clouds (c.f. Ward et al. 2016) and compared to the Milky Way (Cooper et al. 2013). We present near-IR integral-field spectroscopy of IR-bright massive YSO candidates in NGC 346 observed with the K-band Multi-Object Spectrograph (KMOS; Sharples et al. 2013) on the Very Large Telescope (VLT) at the European Southern Observatory (ESO). The aim is to confirm their massive YSO nature using near-IR emission features. The sample selection, KMOS observations and data reduction are described in Section 2. Section 3 presents the main results and our analysis, including an overview of the spectra and their emission line fluxes. In Section 4 we discuss the properties of massive YSOs in NGC 346, and compare our results to other near-IR spectroscopic samples of YSOs in the Galaxy and Magellanic Clouds. Finally, we present a summary of our findings in Section 5.

2 OBSERVATIONS

2.1 Target selection

Our targets were selected from the catalogue of Sewilo et al. (2013), who identified 26 high-reliability and 37 possible YSO candidates in NGC 346 using colour-magnitude cuts and fits to spectral energy distributions (SEDs) with YSO models (Robitaille et al. 2006). These classifications are based on: *Spitzer* IRAC (3.6–8.0 μm) and MIPS (24 and 70 μm) data from the SAGE-SMC survey (Gordon et al. 2011), near-infrared (JHK_s) data from the Infrared Survey Facility (IRSF) Magellanic Clouds Point Source Survey (Kato et al. 2007) and the Two Micron All Sky Survey (2MASS; Skrutskie et al. 2006), and optical (UBVI) data from the Magellanic Clouds Photometric Survey (MCPS; Zaritsky et al. 2002) and OGLE-III

(Udalski et al. 2008). Sewilo et al. (2013) define high-reliability YSO candidates as either satisfying multiple YSO colour-criteria or are well-fit with YSO models, whilst possible YSO candidates fulfill at least one colour-magnitude criterion and their environment supports their young nature. All of our targets in NGC 346 were also observed in the mid-IR by Simon et al. (2007) using data from the S³MC survey (Bolatto et al. 2007).

The YSO candidates identified by these galaxy-wide surveys present the first opportunity to study a large sample of embedded YSOs in another galaxy in detail. However, IFU spectroscopy is required to confirm that these objects are indeed single massive YSOs, or if multiples are detected to conclusively identify the massive YSOs from other sources in the compact proto-cluster (see e.g., Carlson et al. 2012). To ensure a sufficiently high signal-to-noise (S/N) ratio and line detection rate in our spectroscopy we made a cut in the *J*-band luminosity of $> 0.08 \text{ mJy}$ in the NGC 346 catalogue from Sewilo et al. (2013). From this list of YSO candidates, 18 were observed with KMOS, with the final target selection defined by the KMOS arm allocation software KARMA (Wegner & Muschielok 2008). Priority was given to the high-reliability YSO candidates, with the possible high-mass YSO candidates used as fillers. In total 15 high-reliability and 3 possible YSO candidates were observed.

A summary of the observed targets and their physical properties is given in Table 1, including masses and luminosities from Sewilo et al. (2013) or, in the case of Y519, Y545 and Y548, from Simon et al. (2007), which were derived by fitting their SED with YSO models from Robitaille et al. (2006). Their locations are shown in Figure 1 on a $\text{H}\alpha$ image obtained with the VLT FORS1 instrument on 1999 August (PI: Tolstoy; 063.N-0560). The majority of our candidate protostars are concentrated along the bright dust ridges/filaments in the main H II region. In three instances no values were provided in the literature for the source luminosity. In these cases we derive an estimate for the bolometric luminosity via a simple trapezoidal integration of the SED. This method has been used by Woods et al. (2011), Ruffle et al. (2015) and Jones et al. (2017) for sources at all evolutionary stages including YSOs in both the LMC and SMC.

2.2 KMOS observations

KMOS is an integral-field spectrograph with 24 deployable integral-field units (IFUs) that can be deployed across a $7.2'$ field on the sky. Each IFU has a field-of-view of $2.8' \times 2.8'$, sampled by 14×14 spatial pixels (spaxels), i.e. each spaxel has an angular size of $0.2''$. Medium-resolution ($R = 3000\text{--}4000$) YJ, H and K band spectra of the 18 candidate YSOs were obtained with KMOS over two nights on 2018 Sep 28–29 (PI: Jones; 0101.C-0612(A)), with total science integrations of 8400s, 1620s and 3480s in the YJ, H and K bands. The observations were taken in good conditions, with a typical seeing of $< 0.8''$. Offset sky frames were obtained using a standard object-sky-object pattern, with each integration dithered to improve bad-pixel rejection from the final extracted spectra. Standard stars were also observed throughout both nights for telluric correction.

2.3 Data reduction

The KMOS IFU datacubes were reduced using the ESO pipeline (version 2.6.3) provided as part of the ESO Reflex automated data reduction environment (Freudling et al. 2013; Davies et al. 2013). This flat fields, wavelength calibrates, and telluric corrects the raw data, including removing atmospheric absorption using MOLECFIT

Table 1. Summary of VLT-KMOS targets in NGC 346. Luminosities, temperatures and mass estimates are from [Sewilo et al. \(2013\)](#) from SED model fits (except for Y519, 545 and Y548 which are from [Simon et al. 2007](#)). If a target was poorly fit by the SED models the bolometric luminosity was estimated from the SED over the range of the available photometry.

ID	RA [deg]	Dec [deg]	J [mag]	H [mag]	K [mag]	L_{star} [L_{\odot}]	T_{star} [K]	M_{star} [M_{\odot}]	M_{env} [M_{\odot}]	M_{disc} [M_{\odot}]	Evol. Stage
Y519	14.66801	-72.15031	19.47	19.08	17.32	1590	...	6.0	II
Y523	14.70647	-72.17622	17.77	16.69	16.68	13400	6170	15.5	3280	0.0445	I
Y524	14.72361	-72.16790	15.99	15.61	14.38	4190	5420	11.3	1250	1.6	I
Y525	14.73176	-72.14223	17.53	16.56	15.74	8580	27000	11.0	1.40E-06	0.265	II
Y528	14.73779	-72.20974	19.70	18.32	17.42	5910	25500	9.84	0.000613	4.93E-07	III
Y532	14.76068	-72.16866	16.08	15.30	14.24	5180	12700	9.71	198	0.0356	I
Y533	14.76242	-72.17651	14.93	14.90	14.97	4940	...	7.8
Y535	14.77266	-72.17653	14.49	13.44	12.13	27200
Y538	14.78580	-72.18427	17.19	16.33	15.88	6000	18800	8.44	13.4	0.00174	I
Y543	14.79897	-72.20679	18.90	18.63	17.12	40400	5600	21.4	6250	0	I
Y544	14.80103	-72.16624	15.15	14.57	13.63	3240	7100	10.1	21.3	1.92	I
Y545	14.80886	-72.15774	15.43	15.29	14.78	8380	...	11.0	II
Y547	14.81283	-72.18440	15.17	14.81	13.34	3580	8050	10.5	25	0.0111	I
Y548	14.82079	-72.15431	16.81	15.99	15.34	653	...	5.5	II
Y549	14.82146	-72.19002	17.09	16.41	15.82	14200	29400	13.1	62.5	0.254	II
Y551	14.82924	-72.15842	19.18	18.44	14.83	392	8840	5.13	39.6	0.0249	I
Y553	14.83529	-72.18928	16.66	16.16	15.47	6150
Y556	14.84927	-72.21566	17.50	17.22	16.68	5910	25500	9.84	0.000613	4.93E-07	III

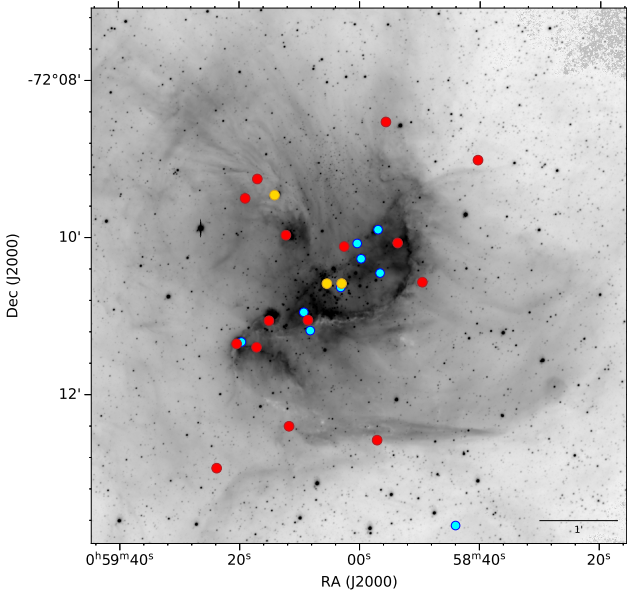


Figure 1. $H\alpha$ FORS1 map of NGC 346 with north pointing up and east to the left. The location of the high-reliability YSO candidates from [Sewilo et al. \(2013\)](#) observed with KMOS are shown in red, with the remaining unobserved high-reliability candidates shown in cyan. Three ‘possible’ YSO candidates marked with gold symbols from [Sewilo et al.](#) were also observed using otherwise unallocated KMOS arms.

([Kausch et al. 2015](#); [Smette et al. 2015](#)). Sky subtraction using a classic nod-to-sky sequence was also performed using the KMOS pipeline. Standard star observations were reduced in an identical manner to the science data; these are then used to flux calibrate the science datacubes.

To determine the precise location and number of sources in

each of our data cubes we use the python DAOSTARFINDER function ([Bradley et al. 2021](#); [Stetson 1987](#)) to detect point sources in the collapsed continuum image. Initially we set the detection threshold at the 3-sigma noise level above the median absolute deviation to determine if the *Spitzer* YSO candidate is a member of a compact cluster, and then increased this threshold to the 5-sigma level to determine a source list for spectral extraction. The full list of sources, their positions and the bands they were detected in are given in Table A1. As found from higher angular-resolution follow-up of other YSOs in the Clouds identified with *Spitzer* (e.g. [Chen et al. 2009](#)), many of our *Spitzer* targets (~50%) are resolved into multiple sources in the KMOS data-cubes. This is not surprising given the seeing of our observations (<0''.8) compared to the angular resolution of IRAC (1''.8). Indeed, we identified multiple sources (using the 3-sigma cut) in half (9/18) of our targets.

One-dimensional science spectra were obtained using aperture extraction for each point-source observed in the data cubes. A circular aperture with a 2-pixel radius was used, centred on the peak of the source to ensure the signal is dominated by stellar emission and to minimise the background contribution. A larger annulus scaled to the same area of the aperture was used to measure and subtract the local background. For each extracted spectrum we estimated its S/N from a set line-free region for each band using the SNR function from the SPECUTILS python package ([Earl et al. 2022](#)). Only spectra with S/N > 10 were retained for further analysis. In total we extracted 26 YJ, H or K band spectra for 12 sources to which we applied a seven-pixel boxcar smoothing filter.

3 RESULTS

With the KMOS IFU we observed 18 high-mass YSO candidates identified from *Spitzer* data. In these datacubes multiple components can be present. In this section, we analyze the 15 sources in the datacubes that have a 5- σ detection from the collapsed continuum images and thus extracted spectra. Of these 12 sources have spectra

Table 2. RA and Dec (J2000) for each source with a $>5\sigma$ detection in the KMOS K-band images. Those with extracted KMOS spectra with $S/N > 10$ in the YJ, H and K regions are indicated in the final three columns.

ID	RA [deg]	Dec [deg]	S/N > 10 spectra		
			YJ	H	K
Y525A	14.73175	-72.14212	✓
Y532A	14.76073	-72.16867	✓	✓	✓
Y533A	14.76206	-72.17640	✓	✓	✓
Y535A	14.77241	-72.17649	✓	✓	✓
Y538A	14.78541	-72.18408	✓
Y544A	14.80079	-72.16629	✓	✓	✓
Y544B	14.80131	-72.16624	✓
Y545A	14.80875	-72.15780	✓	✓	✓
Y548A	14.82105	-72.15406	✓	...	✓
Y549A	14.82122	-72.18994	✓
Y553A	14.83569	-72.18915	✓	...	✓
Y556A	14.84910	-72.21564	✓	✓	✓
Y524A	14.72315	-72.16779
Y528A	14.73675	-72.20973
Y543A	14.79879	-72.20650
Y551A	14.83005	-72.15836
Y551B	14.82900	-72.15835

with a signal-to-noise ratio ($S/N > 10$) sufficient for reliable line detection and measurement.

3.1 Continuum emission

Continuum maps for the YJ-, H- and K-band data-cubes are shown in Figures ??–??, which were generated by summing the spaxels along the wavelength axis of the cubes. With such images we can examine the immediate surroundings of the IRAC-identified YSOs, and identify multiple faint sources.

In our sample of 18 YSO candidates identified by [Sewilo et al. \(2013\)](#), Y544 and Y551 are clearly resolved into two sources over multiple bands. Seven other candidates also show evidence of multiplicity (see Table A1), although the companion sources are generally faint and in most cases we are unable to reliably measure their properties and astrometric positions. The RA and Dec (J2000) of each extracted source (with at least a $5\text{-}\sigma$ detection in the continuum data) are given in Table 2. The positions are determined from the KMOS K-band continuum images. Multiple sources within the same IFU are denoted by "A" or "B" in their name.

In each field we also searched for spatially-extended line emission beyond the continuum sources. No significant Br γ emission or H $_2$ emission was detected in the moment zero maps outside of the compact source region. This lack of notable extended emission is likely due to a difference in the spatial resolution between KMOS and high spatial resolution adaptive-optic IFU instruments like VLT/SINFONI (Spectrograph for INtegral Field Observations in the Near Infrared). With SINFONI (spatial resolution of 0.1–0.2 arcsec), [Ward et al. \(2017\)](#) detect spatially extended Br γ or H $_2$ emission towards approximately half their YSO sample in the SMC. This is a factor of 6 better sampled than our seeing-limited KMOS data and may explain the difference.

3.2 Properties of the spectra

The KMOS spectra of the 12 sources (with $S/N > 10$) provide (partial) coverage over $\sim 0.8 - 2.5 \mu\text{m}$. Six sources were detected in all

Table 3. Common emission lines in the KMOS spectra ($>3\sigma$ detections) and their detection frequency within our sample. Note that we do not have sufficiently good spectra (i.e. $S/N > 10$) for each source in each KMOS band; to account for those with limited spectral coverage detections are presented relative to the total number of spectra in each band.

Emission Feature		Wavelength (μm)	Number of Sources
Brackett 7-4	Br γ	2.166	9 of 11
H $_2$ 1-0:S(1)		2.128	7 of 11
Paschen 5-3	Pa β	1.282	6 of 9
Paschen 6-3	Pa γ	1.094	6 of 9
H $_2$ 1-0 S(0)		2.224	5 of 11
Brackett 10-4		1.737	5 of 6
Brackett 11-4		1.681	4 of 6
Brackett 12-4 / [Fe II]		1.641	4 of 6
Fe II /H $_2$ 1-0 S(9)		1.689	4 of 6
[Fe II]		1.257	4 of 9
He I		1.083	4 of 9

three KMOS bands, three have only $S/N > 10$ in the K-band and one (Y525A) has only $S/N > 10$ in the YJ-band. The nine YJ band, six H band, and eleven K band spectra of the twelve YSO candidates are shown in Figures 2 – 4 (and the bands in which each source is detected are summarised in Table 2).

Massive YSOs typically have hydrogen recombination lines (e.g. Br γ) and H $_2$ lines in their spectra, H II regions have strong H I emission, and O-type spectra can be identified from the ratio of He I to He II absorption lines. To assess the evolutionary status of each source the KMOS spectra were therefore classified where possible as either YSOs or early-type stars according to the shape of their continuum and the emission and/or absorption features present in their spectra.

3.2.1 Observed emission lines

The KMOS spectra show a rich variety of emission lines from atomic and molecular species. In the YJ-band strong Paschen series transitions from Pa γ (Pa 6-3, $1.094 \mu\text{m}$) and Pa β (Pa 5-3, $1.282 \mu\text{m}$) dominate the spectra. Hydrogen recombination lines from the Brackett series are prevalent in the H-band, with the strongest (secure) detection being Br 10-4 at $1.737 \mu\text{m}$ (the Br 9-4 line is stronger but lies near the edge of the observed range, where line measurements have larger uncertainties due to noise). A number of H $_2$ lines are also present, as is emission from shocked [Fe II] at $1.644 \mu\text{m}$. Finally in the K-band, the most prominent feature is from Br γ (Br 7-4) emission at $2.16 \mu\text{m}$, with other atomic hydrogen lines from the weaker Pfund series also present. Table 3 summarises the observed emission lines (with at least 3σ detections) and their detection frequency within our sample. A full listing of lines detected in each source is given in Table B1. Although there are some weak OH-line residuals after sky subtraction in some of our spectra, we note that our study is helped by the fact that the wavelengths of the strongest sky emission lines do not coincide with the primary diagnostic features for YSOs ([Rousselot et al. 2000](#)).

3.2.2 Emission-line strengths

For each emission line in the extracted 1D spectra we measured the line flux using a Gaussian profile. Spectral lines were initially

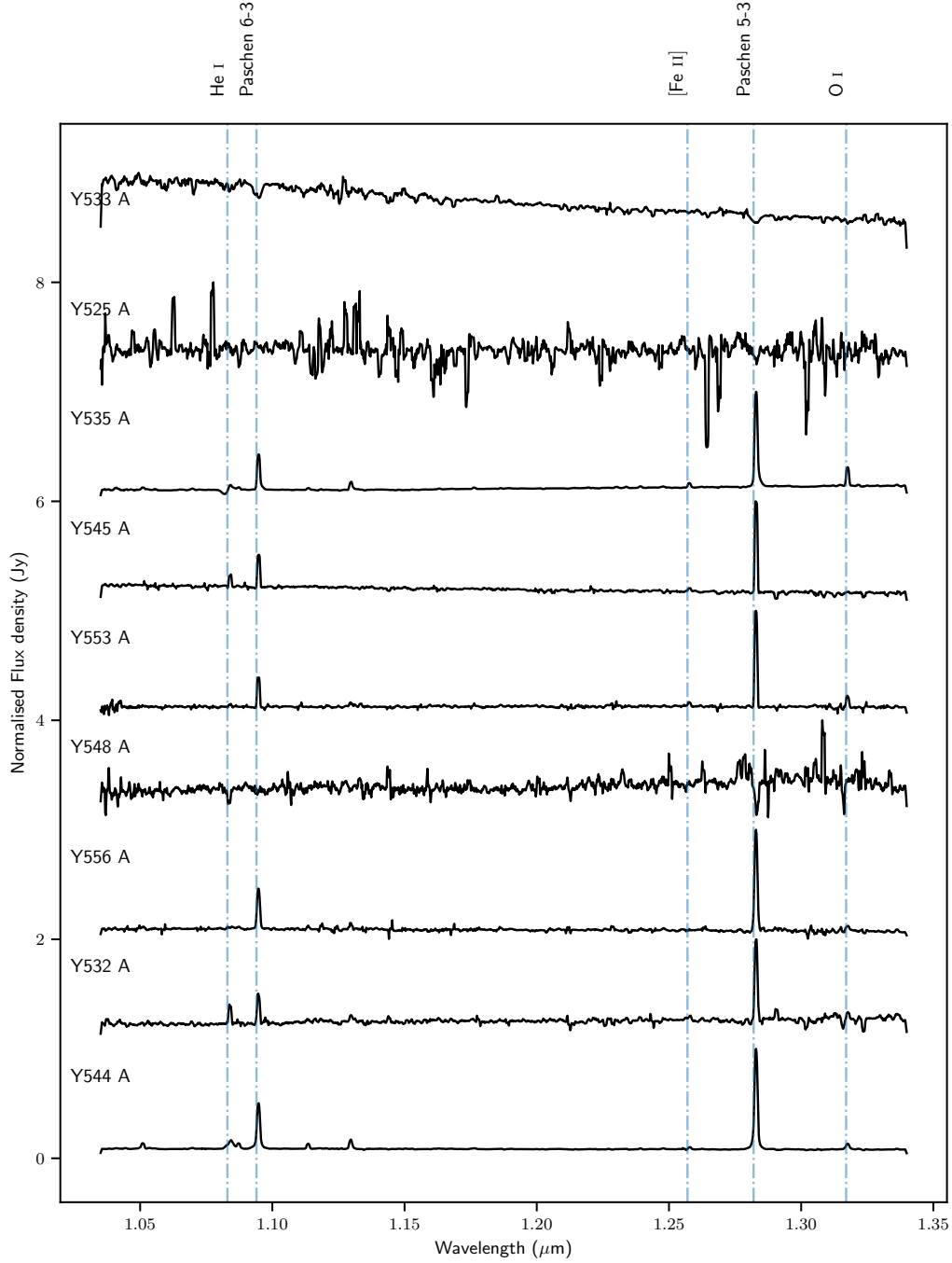


Figure 2. Normalised YJ-Band KMOS spectra with $S/N > 10$ for our YSO candidates. Key emission-lines are marked by the vertical dash-dot lines. For display purposes the flux of each object has been shifted by a continuum unit so the spectra do not overlap.

identified using the `FIND_LINES_THRESHOLD` algorithm from the `SPECUTILS`¹ python package. Only lines with a $> 3\sigma$ detection above the continuum were considered. A local continuum, represented by a third-order polynomial, was then fit to each line region via a Levenberg-Markwardt least-square algorithm and subtracted from the spectra. Finally, the emission-line strength, position and full width at half-maximum (FWHM) were measured for each line by

fitting a Gaussian function to the line profile in the continuum-subtracted spectra. When a line was not detected a 3σ upper limit was estimated using $3 \times F_{\text{noise}} \times \Delta\lambda$, where F_{noise} is the continuum rms noise in the line region and $\Delta\lambda$ is the expected line width, which is assumed to be $0.0014 \mu\text{m}$. Table B1 presents the measured emission line fluxes, these have not been corrected for extinction.

¹ <https://specutils.readthedocs.io/>

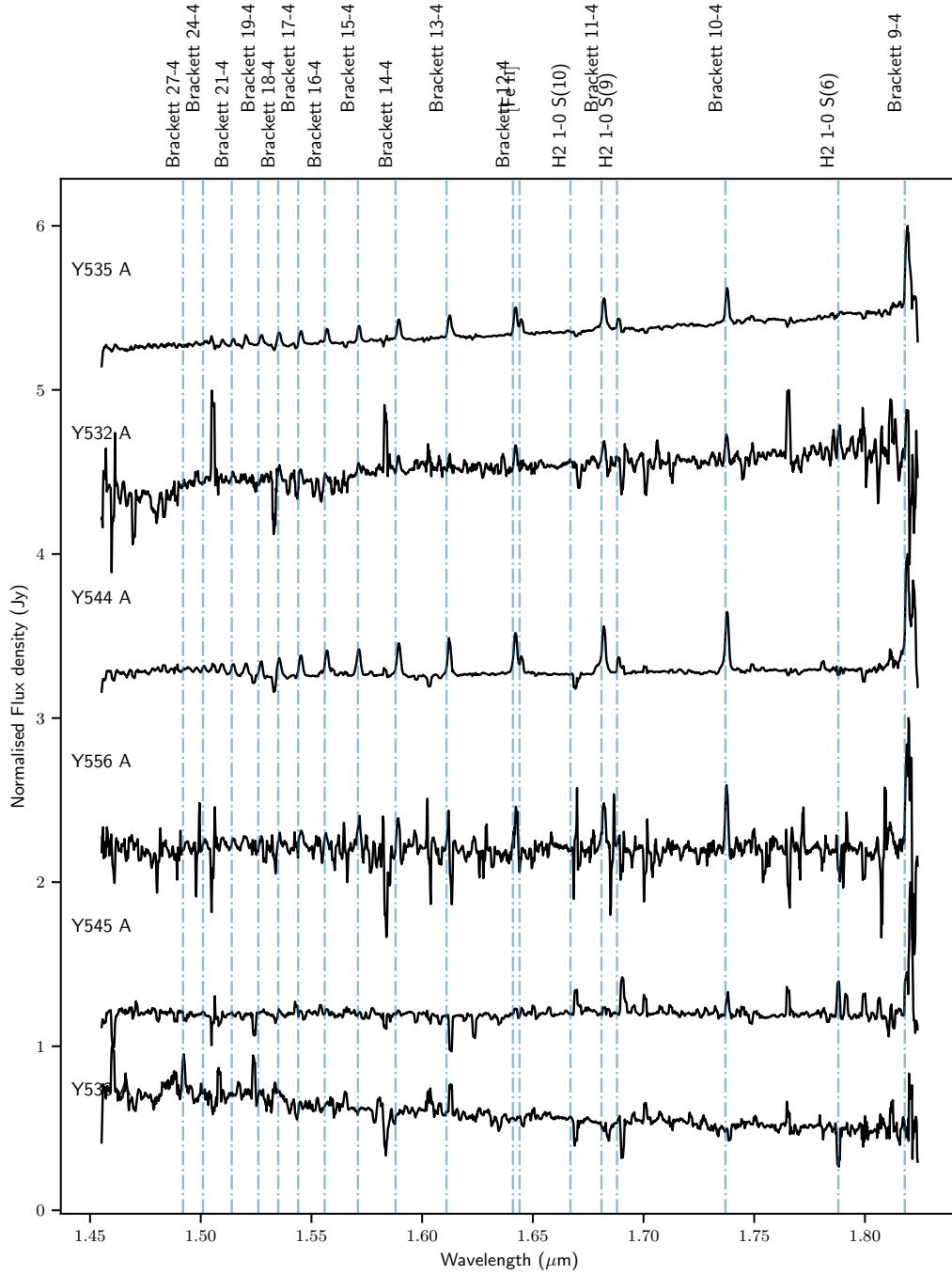


Figure 3. Normalised H-Band KMOS spectra with S/N > 10 for our YSO candidates. Key emission-lines are marked by the vertical dash-dot lines. The spectra between each source are offset by a factor of one.

3.3 Extinction

Extinction can be calculated using line ratios. From the observed $\text{Pa}\beta/\text{Br}\gamma$ line ratio we compute the relative extinction between the wavelengths using:

$$A_{\text{rel}} = 2.5 \times \log \left(\frac{(\text{Pa}\beta/\text{Br}\gamma)_{\text{obs}}}{(\text{Pa}\beta/\text{Br}\gamma)_{\text{exp}}} \right) \quad (1)$$

where ‘obs’ and ‘exp’ are the observed and expected flux ratios. Assuming Case B recombination which is valid for $100 < n_e < 10^4 \text{ cm}^{-3}$ and $5000 < T_e < 10^4 \text{ K}$ (Storey & Hummer 1995), the

intrinsic flux ratio should be $\text{Pa}\beta/\text{Br}\gamma = 5.75 \pm 0.15$. The relationship between the relative extinction due to dust attenuation and $E(B-V)$ is given by:

$$E(B-V) = \frac{2.5}{k(\lambda_{\text{Br}\gamma}) - k(\lambda_{\text{Pa}\beta})} \log_{10} \left[\frac{(\text{Pa}\beta/\text{Br}\gamma)_{\text{obs}}}{(\text{Pa}\beta/\text{Br}\gamma)_{\text{int}}} \right] \quad (2)$$

where $k(\lambda_{\text{Br}\gamma})$ and $k(\lambda_{\text{Pa}\beta})$ are the reddening curves evaluated at the $\text{Br}\gamma$ and $\text{Pa}\beta$ wavelengths, respectively. Here we use the extinction curves for the SMC derived by Gordon et al. (2003), and adopt $R_V = 2.74$ which is the average value for the SMC bar. The

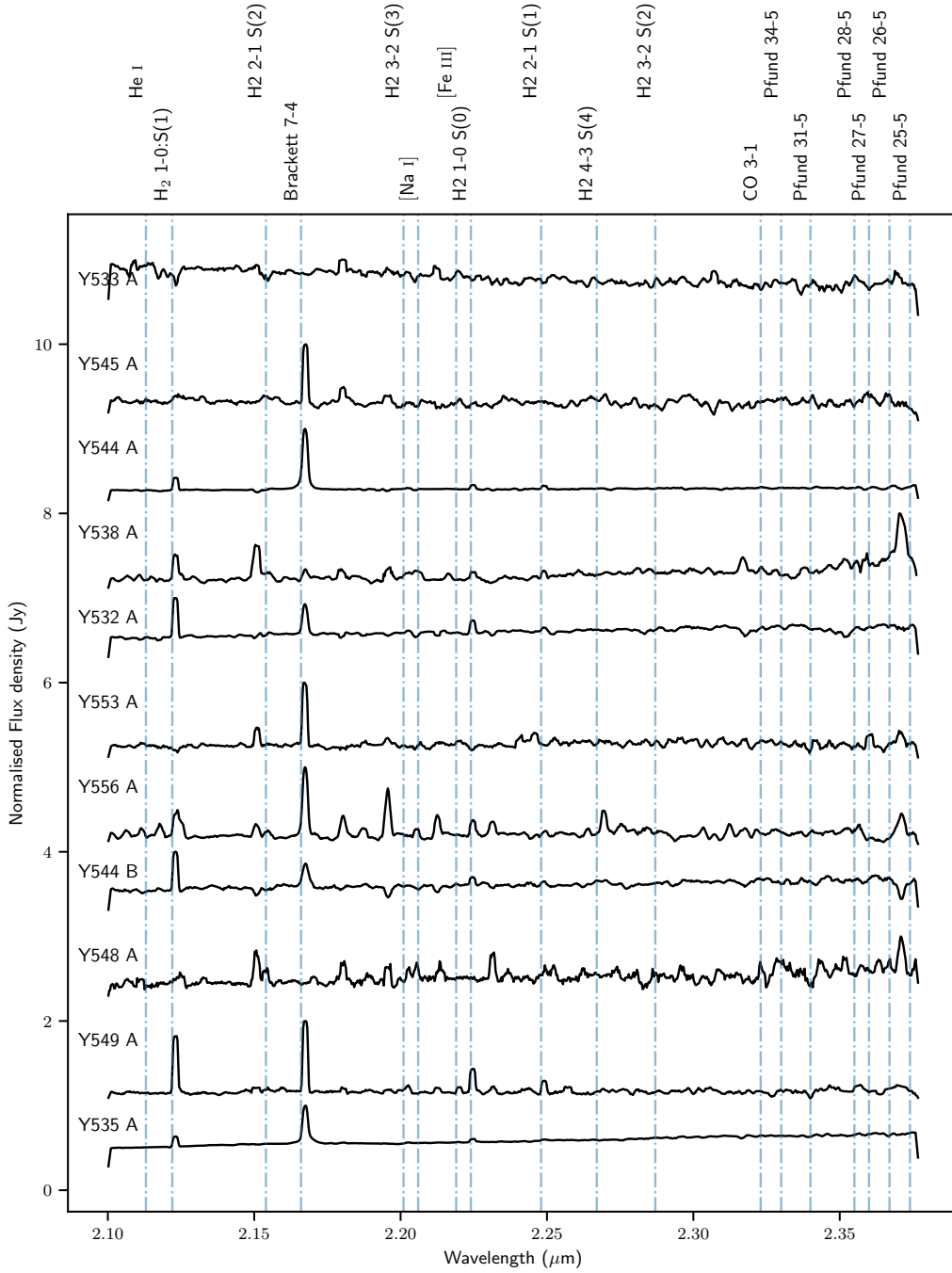


Figure 4. Normalised K-Band KMOS spectra with $S/N > 10$ for our YSO candidates. Key emission-lines are marked by the vertical dash-dot lines. The spectra between each source are offset by a factor of one.

choice of R_V affects the shape of the extinction curve, and literature values for the SMC range between 2.05 – 3.30, with higher values resulting in increased A_V values. The computed $E(B - V)$ and A_V values are given in Table 4. Robust estimates for either (or both) lines were not possible in three sources with YJ and K band spectra, namely: Y544B, Y548A, and Y549A. This leaves the 6 sources with $\text{Pa}\beta$ values listed in Table 3 with extinction measurements listed in Table 4.

Extinction corrections were calculated for each emission line individually. The A_λ extinction in magnitudes at the wavelength λ

is given by:

$$A_\lambda = k(\lambda)E(B - V). \quad (3)$$

The intrinsic luminosity of each line, L_{int} , is then obtained from:

$$L_{\text{int}}(\lambda) = L_{\text{obs}}(\lambda)10^{0.4A_\lambda}, \quad (4)$$

where the observed line luminosities L_{obs} are calculated assuming a distance to the SMC of 62.44 ± 0.47 kpc (de Grijs & Bono 2015). For more details on relating hydrogen recombination lines to

Table 4. Extinction estimates for sources with robust determinations of the Pa β and Br γ line intensities.

ID	Pa β /Br γ	$E(B - V)$ [mag]	A_V [mag]
Y532A	2.044 ± 0.336	1.28 ± 0.21	3.51 ± 0.92
Y535A	3.307 ± 0.137	0.68 ± 0.06	1.86 ± 0.16
Y544A	4.146 ± 0.375	0.40 ± 0.12	1.10 ± 0.33
Y545A	5.596 ± 0.258	0.03 ± 0.06	0.08 ± 0.16
Y553A	3.370 ± 0.156	0.66 ± 0.07	1.81 ± 0.19
Y556A	4.389 ± 0.145	0.33 ± 0.05	0.90 ± 0.14

attenuation due to dust see e.g., [Calzetti et al. \(2000\)](#) and [Momcheva et al. \(2013\)](#).

The median extinction for our sources is $A_V = 1.54 \pm 0.48$. This is comparable to the values [Ward et al. \(2017\)](#) obtained in the optical emission for YSOs in the SMC, but significantly lower than their mean extinction values calculated from lines solely in the K-band. This suggests that Pa β /Br γ ratio samples a shallower region of the YSO environment compared to estimates using the H $_2$ Q-branch. The visual extinctions towards our sample are also relatively low compared to estimates from broadband photometry for massive YSOs in the Galaxy ([Cooper et al. 2013](#)) and the LMC ([Ward et al. 2016](#)). Compared to the most extreme sources in these samples our spectra have relatively flat continua and do not show strong dust extinction; consistent with lower dust-to-gas ratios in the SMC. Furthermore as the hydrogen recombination lines arise from optically thin regions of a YSO, they do not provide a complete picture of extinction in that source and the true value for extinction is probably much higher, thus rendering direct comparisons to the broadband estimates invalid.

H $_2$ Q-branch lines together with S-transition lines can also be used to evaluate A_V (e.g. [Davis et al. 2011](#)). However, the Q-branch lines occupy a region of the K-band spectrum which is particularly noisy, preventing reliable line ratios to estimate extinction for our sample using this method. Likewise, estimates of A_V via [FeII] transitions in the J and H-bands are limited by the potential blend of the Br 10 line and [FeII] at $1.64\mu\text{m}$.

3.4 Stellar radial velocities

Radial velocities (v_r) of our targets were measured from the Doppler shifts of the Br γ , H $_2$ 1-0:S(1), Pa γ and Pa β lines. The line centres were measured by Gaussian profile fits to the emission lines detected with strengths $>3\sigma$ above the continuum. Mean velocities and standard deviations (δv_r) of the individual measurements are given for the eight sources where estimates were possible in Table 5. The average radial velocity for our targets is $178 \pm 3 \text{ km s}^{-1}$, in good agreement with the peak velocity of the H I gas emission in the direction of NGC 346 (see, e.g. [Stanimirovic et al. 1999](#)). The mean velocity also compares well with the systemic velocities of massive OBA-type stars in this region (e.g. [Evans et al. 2006](#); [Evans & Howarth 2008](#); [Dufton et al. 2020](#)), which are notably offset by $\sim 20 \text{ km s}^{-1}$ compared to older stellar populations in the SMC (e.g. [Harris & Zaritsky 2006](#)).

3.5 Comments on individual sources

We see Br γ emission in 9 of the 11 K-band spectra in our sample. This is consistent with massive YSOs that have ionized their gas

Table 5. Mean radial velocity (v_r) estimates for each source.

ID	v_r [km s $^{-1}$]	δv_r [km s $^{-1}$]
Y532A	174.34	2.58
Y535A	181.78	0.91
Y544A	176.05	3.49
Y544B	189.38	9.73
Y545A	187.65	1.90
Y549A	183.95	1.04
Y553A	159.46	2.27
Y556A	171.82	1.57

and is indicative of their youthful nature, confirming the YSO photometric classifications from [Sewilo et al. \(2013\)](#) and [Simon et al. \(2007\)](#). Of particular note are the three sources with only K-band spectra, as they may be located deep inside dense molecular clouds or are still embedded in in-falling envelopes.

We first briefly discuss the two sources without Br γ emission:

- **Y533A:** There is a small offset in the position, but the brightest source in this cube is a O7 dwarf previously observed spectroscopically by [Massey et al. \(1989, NGC 346 MPG 396\)](#) and [Dufton et al. \(2019, NGC346-1015\)](#). There is a faint companion star nearby in the data cube which is perhaps the source of the large *Spitzer* IR excess, giving an offset positional centroid compared to the O7 star. Secure line identifications are difficult in the KMOS data, but Pa β and Pa γ absorption are present in the YJ-band spectrum, with a hint of He I 1.083 μm absorption. In the H- and K-band spectra the absence of strong absorption lines from the Brackett series is surprising, but we are perhaps limited by the S/N of the data. There are tentative detections of He II 1.572 and 1.692 μm , but these are somewhat suspicious given the absence of Brackett absorption lines, as well as the absence of He I 1.700 μm (see, e.g. [Blum et al. 1997](#); [Hanson et al. 2005](#)). In short, the YJ-band spectrum is consistent with Y533A being NGC 346 MPG 396, but it is difficult to say much more with the current near-IR data.

- **Y548A:** Secure line identifications are also challenging for Y548A. There is a more secure detection of He I 1.083 μm absorption, with (noisy) absorption present at the wavelength of Pa β , but notably with no corresponding detection of Pa γ . If the Pa β absorption is real, it would suggest a cooler object than Y533A; analogous to an early spectral type, between late O and early B.

We now discuss three other sources of note:

- **Y535A:** Identified as NGC 346 MPG 454, Y535A is located in the very central part of the NGC 346 complex. Y535A is an intriguing object. It is among the most luminous sources in the region at both X-ray and near-IR wavelengths ([Nazé et al. 2002](#); [Rubio et al. 2018](#)). Furthermore, it appears to be part of a young star complex, with a mid-infrared spectra (listed as SMC IRS 18 and PS9 in [Ruffle et al. 2015](#) and [Whelan et al. 2013](#), respectively) dominated by a massive YSO exhibiting silicates in emission ([Whelan et al. 2013](#); [Ruffle et al. 2015](#); [Kraemer et al. 2017](#)). Representing the most evolved YSO type in their schema (see [Woods et al. 2011](#) for a in depth description and [Oliveira et al. 2013](#) for the first adaption of this classification scheme to the SMC) Y535A is considered to be a YSO-4 (Herbig AeBe star) by [Ruffle et al. \(2015\)](#) from its *Spitzer* Infrared Spectrograph (IRS) data and is spectroscopically classified as a Be star by [Martayan et al. \(2010\)](#) in their slitless H α survey. It is likely that multiple nearby sources are contributing to the observed

flux that cannot be separated out. This bright compact star cluster is surrounded by many young massive stars. High-resolution *HST* data reveal nine stars within $1''$ of its extracted position (Sabbi et al. 2007), however these sources are unfortunately too faint to be detected in our KMOS data cubes, where Y535A appears as a single object in the H and K bands, with a possible companion detected at the $3\text{-}\sigma$ level in YJ.

According to Rubio et al. (2018) Y535A (also known as ‘Source C’) is a Stage I YSO, with a mass of $18 M_{\odot}$ enshrouded by a compact H II region. Their ‘Source C’ HK-band ($R \sim 1000$) spectrum is rich in hydrogen recombination, H_2 and He I emission lines. The detected lines and rising continuum towards longer wavelengths in the data from Rubio et al. are consistent with our near-IR spectra, which exhibits a P-Cygni profile in He I $1.083 \mu\text{m}$ that suggests an outflow. Fluorescent Fe II at $1.6878 \mu\text{m}$, which originates in discs (Zorec et al. 2007), is present in both the KMOS data and the HK spectra from Rubio et al. However, we do not detect extended Br γ or H_2 emission from the source (see Section 3.1). Combined, the results confirm the massive YSO nature of Y535A.

- *Y544A & B*: Appearing as single sources in *Spitzer* data this target was resolved into multiple objects with the KMOS IFU (and in high-resolution *HST* images; Hennekemper et al. 2008). This YSO candidate was observed with the *Spitzer* IRS (Ruffle et al. 2015, SMC IRS 21). SMC IRS 21 was classified as a YSO-4: a Herbig Ae/Be type object due to the silicate emission features present (Whelan et al. 2013; Ruffle et al. 2015). The position of this YSO candidate coincides with that of NGC 346 MPG 605, a red star with $(B - V) = 0.25$ mag from Massey et al. (1989), which has also been classified as a Be-type star, NGC 346:KWBBE 448 with a B0 spectral type (Keller et al. 1999; Martayan et al. 2010).

In the KMOS data, both Y544A and Y544B have comparatively flat continua, with no excess dust emission at $\lambda > 2.3 \mu\text{m}$. Y544A has spectral detections in all three KMOS bands, however, Y544B only has a K-band spectrum with $S/N > 10$, suggesting this is the cooler object and/or with larger extinction than Y544A. Fluorescent Fe II and [Fe II] lines are observed in Y544A compatible with forbidden disc emission potentially from a Herbig Oe/Be disc.

4 DISCUSSION

4.1 H II emission

Hydrogen recombination lines (e.g., Br γ , $n = 7 - 4$ at $2.166 \mu\text{m}$) are a primary diagnostic for the physical properties and kinematics of ionized regions. Our spectra are rich in Paschen, Brackett, and Pfund series emission lines. The Br γ line is the strongest H II emission line in the K-band associated with YSOs, with a detection frequency of 80% in our sample. It is commonly used to trace accretion luminosity (e.g. Calvet et al. 2004; Mendigutía et al. 2011; Cooper et al. 2013; Ward et al. 2016, 2017; Reiter et al. 2019) in protostars (especially in sources which are heavily extincted) via the relation:

$$\log \frac{L_{\text{acc}}}{L_{\odot}} = (0.91 \pm 0.27) \times \log \frac{L_{\text{Br}\gamma}}{L_{\odot}} + (3.55 \pm 0.80). \quad (5)$$

Metallicity is not expected to influence this relation, as the number of photons capable of ionising hydrogen (at $T > 10^4$ K) in metal-poor environments is comparable to solar metallicity values (Kudritzki 2002).

The extinction-corrected luminosities of Br γ emission compared to the bolometric luminosity of each source are shown in

Figure 5. Treating the luminosity from the *Spitzer* YSOs as single massive objects is a reasonable assumption as the SED of a compact-(proto)cluster is dominated by its most massive star (e.g., Bernasconi & Maeder 1996; Chen et al. 2009). For the *Spitzer* sources that we resolved into multiple continuum sources, the bolometric luminosity is considered an upper limit. We also plot the relation from Mendigutía et al. (2011, equation 5) for a range of L_{bol} ; most of our objects fall in the $0.01 L_{\text{bol}} < L_{\text{acc}} < 0.1 L_{\text{bol}}$ range.

The Pa 5-3 and 6-3 lines are seen in emission in six of the nine objects with YJ spectra. In the H-band there are three strong Brackett series transitions (12-4 at $1.64 \mu\text{m}$, 11-4 at $1.68 \mu\text{m}$ and 10-4 at $1.74 \mu\text{m}$) in several sources, with multiple higher-order lines in the Brackett series also present. Pfund series emission is detected in four sources, however this region of the spectrum has a high degree of noise due to the poor atmospheric transmission. Obtaining accurate flux measurements for these lines is therefore challenging and we do not use them in our analysis.

The Br γ luminosities for our NGC 346 sample are compared in Figure 6 to results for high-mass galactic YSOs discovered in the Red MSX Source (RMS) survey (Cooper et al. 2013) and high-mass YSOs in the Magellanic Clouds (Reiter et al. 2019; Hutsemekers 1994; Ward et al. 2016, 2017; Rubio et al. 2018)². Our results are consistent with those for Galactic YSOs, and are at the fainter end of spectroscopic sources observed in the Magellanic Clouds; especially when compared to the LMC samples which have on the whole higher L_{bol} values. Furthermore, the LMC sample includes H72.97–69.39 one of the most luminous YSOs in the LMC, which has also been proposed to be a young super star cluster analogous to R136 in the heart of 30 Dor (Ochsendorf et al. 2017; Reiter et al. 2019). If, as expected, the Br γ luminosity is correlated to the mass of the YSO, then our objects would sample the lower-mass end of the massive YSO distribution (i.e. more likely the progenitors of B-type rather than O-type stars).

To compare the SMC and Milky Way samples with luminosities in the range $1\text{--}50 \times 10^3 L_{\odot}$ in a quantitative manner, we divide each sample into three luminosity bins split equally in logarithmic space. In general, the mean and median Br γ line strengths increase as the bolometric luminosity of the source increases, and for a given luminosity range the mean and median Br γ luminosity is lower for the SMC sources compared to the Milky Way sources. However, this trend has considerable scatter and large associated errors, due to the low number of sources in each bin and the large uncertainties associated with the bolometric luminosity. To determine if this effect is real and a consequence of the differences in the metallicity between the populations will require additional high-spatial resolution observations (now possible by *JWST*) to place better constraints on both the bolometric luminosity and to reduce potential statistical biases in the samples.

4.2 H₂

Molecular hydrogen emission lines are commonly observed in dense photodissociation regions and are also a common tracer of shocks from outflows. Large energies ($T > 10^3$ K) are required to excite H_2 . The detection of H_2 emission is prevalent in massive objects in the earliest stage of star formation where bipolar molecular outflows are common. At later stages, the detection rate of H_2 drops as the

² No line strengths are published for the 10 massive YSOs spectroscopically identified by van Gelder et al. (2020) in the 30 Doradus region of the LMC.

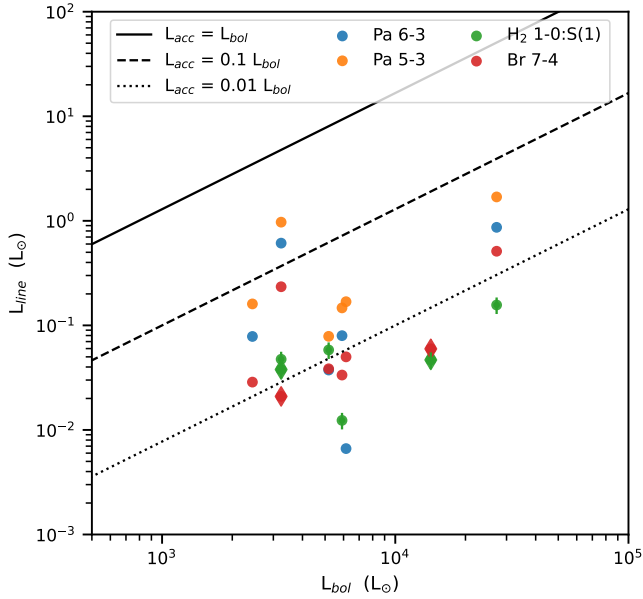


Figure 5. Line luminosity vs. bolometric luminosity (for $>3\sigma$ line detections), in which the line luminosities have been corrected for extinction where possible (circles); uncorrected lines are plotted as diamonds. The error bars for the Br γ , Pa γ and Pa β lines are smaller than the plot symbols. The overplotted lines show the loci of $L_{\text{acc}} = L_{\text{bol}}$, $0.1 L_{\text{bol}}$ and $0.01 L_{\text{bol}}$ calculated using the relationship from [Mendigutía et al. \(2011\)](#).

circumstellar envelope dissipates. The H₂ 1-0S(1) line at 2.122 μm is detected in emission in over 60 % of our sample. Other H₂ emission lines are also seen in our sample, although at a reduced rate. A full list of H₂ lines detected in each source is given in Table 3.

The H₂/Br γ ratio can be used to determine excitation conditions in the gas (e.g., [Dale et al. 2004](#); [Yeh et al. 2015](#); [Reiter et al. 2019](#)). Two objects (Y532A and Y544B) have a H₂/Br γ ratio slightly greater than unity, suggesting shocks excited by protostellar outflows are contributing to the observed flux. These two objects are likely the youngest sources in our sample. For the remainder of the sample H₂/Br γ < 1 , suggesting photoexcitation is the primary mechanism. However, given the number of H₂ lines detected towards the objects in our sample, the distribution in line ratios and the uncertainties in these measurements, the true excitation mechanism is likely a combination of both photoexcitation and shock excited processes representing a complex physical environment.

H₂ absorption at 2.122 μm is tentatively seen towards Y533A, a mid O-type star in NGC 346. H₂ absorption lines are relatively weak and are very difficult to observe, requiring unusually hot or radiatively excited gas with sufficiently large column densities ([Lacy et al. 2017](#)). This indicates the star Y533A is still surrounded by its natal gas and dust, or is behind the molecular cloud.

4.3 [Fe II] emission

[Fe II] 1.644 μm emission is often detected in shock-excited gas, including in protostellar jets ([Giannini et al. 2013](#)) and supernova remnants ([Lee et al. 2019](#)). In H II regions far-UV radiation can also excite [Fe II] emission ([Mouri et al. 2000](#)). In the YJ band, [Fe II] at 1.257 μm may be present in Y535A, Y544A, Y545A and Y553A suggesting that these sources have nebular emission. Indeed, [Sewilo](#)

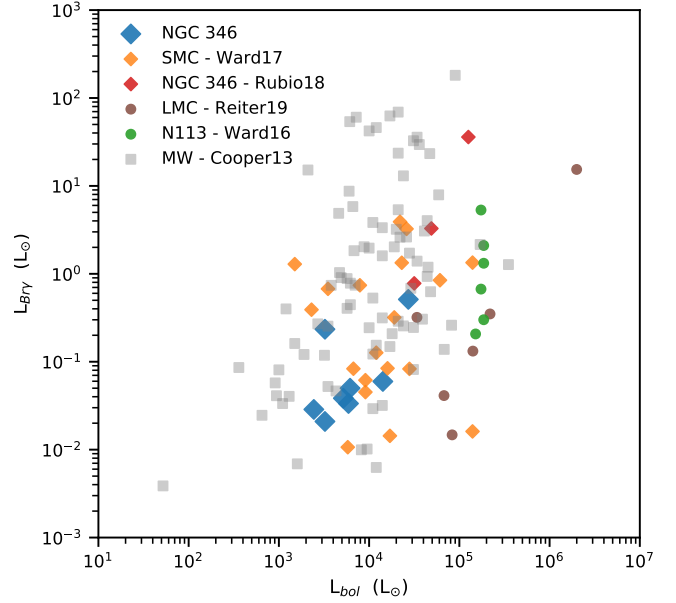


Figure 6. Br γ line luminosity vs. bolometric luminosity for our NGC 346 targets (blue diamonds) compared with published samples: three additional objects in NGC 346 ([Rubio et al. 2018](#), red diamonds), other YSOs in the SMC ([Ward et al. 2017](#), orange diamonds), YSOs in the LMC from [Reiter et al. \(2019\)](#), brown circles) and [Ward et al. \(2016\)](#), green circles) and YSOs in Galactic high-mass, star-forming regions ([Cooper et al. 2013](#), grey squares). For our NGC 346 sample, the error bars for the line luminosity are smaller than the plot symbols. L_{bol} values for the Magellanic Clouds should be treated as an upper limit due to the high prevalence of multiplicity.

[et al. \(2013\)](#) noted that Y545 is surrounded by small H II region in the *HST* H α data.

Shocked [Fe II] lines at 1.644 μm are detected in the H-band spectra of two of our sources, Y535A and Y544A. Unfortunately, at this spectral resolution, quantitative analysis of the [Fe II] is not possible due to blending with the stronger Br 12 line.

4.4 He I emission

He I emission at 1.083 μm is detected in four of the nine sources with YJ band spectra and, as noted earlier in Section 3.5, displays absorption in Y533A and Y548A. To ionize helium hard UV photons are needed, suggesting that only the brightest sources with temperatures $> 20,000$ K can directly excite the line. However, collisional excitation of He I emission from a stellar wind is also possible, explaining why He I emission is frequently observed around low- and intermediate-mass T-Tauri and Herbig AeBe stars (e.g., [Edwards et al. 2006](#); [Fischer et al. 2008](#); [Reiter et al. 2018](#)). The detection of He I emission in our sample cannot therefore be used to constrain the either the mass or evolutionary stage of these objects ([Covey et al. 2011](#); [Connelley & Greene 2014](#)). Conversely, He I can only be seen in absorption when the source has kinetic temperatures above $T \geq 10^4$ K and electron densities of $n_e \geq 10^8 \text{ cm}^{-3}$ ([Drew et al. 1993](#)), thus the line must be produced very close to a hot star (partly the reason for our earlier classifications of Y533A and Y548A as early-type stars).

One source, Y535A, shows a P-Cygni-type profile at He I 1.083 μm , with blue-shifted absorption and red-shifted emission, characteristic of outflowing gas. He I 1.083 μm profiles have

been used to trace mass flows around low- and intermediate-mass stars (e.g. [Edwards et al. 2006](#); [Cauley & Johns-Krull 2014](#), respectively). We note that none of our sample displays profiles with the red-shifted absorption characteristic of accretion flows.

4.5 Accretion discs: CO bandhead and fluorescent Fe II

CO overtone bandhead transitions at $2.29\text{--}2.50\ \mu\text{m}$ are commonly observed in galactic YSOs (e.g., [Blum et al. 2004](#); [Bik et al. 2006](#); [Ilee et al. 2013](#)). The distinctive CO bandhead emission originates from the inner part of a Keplerian disc of neutral gas which has high densities ($n > 10^{11}\ \text{cm}^{-3}$) and temperatures (2500–5000 K; [Chandler et al. 1995](#); [Blum et al. 2004](#)). Studies of galactic YSOs show that not all sources with an accretion disc exhibit CO bandhead emission, for instance if the accretion rate is too low or the disc cannot self-shield due to low column densities ([Cooper et al. 2013](#); [Ilee et al. 2018](#)). It is most often detected in sources with moderate mass accretion rates, $\dot{M}_{\text{acc}} \sim 10^5\ M_{\odot}\ \text{yr}^{-1}$. CO bandhead absorption lines arise in a different region, further from the star in the cooler outer envelope ([Davies et al. 2010](#)). Strong CO bandhead absorption is common in the spectra of FU Ori-like objects – low-mass young stars undergoing an accretion outburst (e.g., [Connelley & Reipurth 2018](#)).

We do not detect the CO bandhead in emission or absorption in our data. In the Magellanic Clouds there have only been four tentative or weak detections of CO bandhead emission, with it seen in absorption in two other cases ([Ward et al. 2016, 2017](#); [Reiter et al. 2019](#); [van Gelder et al. 2020](#)). In contrast, 17% of the Galactic YSOs observed by [Cooper et al. \(2013\)](#) show CO bandhead emission. In higher-resolution data of YSOs drawn from the same Galactic sample ($R \sim 7000$ versus $R \sim 500$), the detection rate of CO first overtone emission increased to 34% ([Pomohaci et al. 2017](#)). If we consider all K-band spectroscopic data targeting YSOs in the LMC and SMC (including the KMOS data presented here), the upper-limit to the detection rate for the CO bandhead emission in the Magellanic Clouds is $\sim 7\%$. From a total sample of 53 YSOs in the Clouds, only source #03 in the SMC from [Ward et al. \(2017\)](#) and sources S4, S5-E and S7-A in the 30 Doradus region of the LMC (observed at $R \sim 4000\text{--}17000$; [van Gelder et al. 2020](#)) have discernible CO bandhead emission. In all instances these detections were described as tentative or weak. For instance, for the SMC source #03 of [Ward et al. \(2017\)](#) the 3–1 and 4–2 bandheads have substantial contamination from CO absorption lines and the $\nu = 2\text{--}0$ transition is weak ([Ward et al. 2017](#)). This is the only CO bandhead emission that has been detected in the SMC. This mounting evidence of significantly lower detection rates in metal-poor environments suggests a physical difference between star-formation mechanisms. We discuss this discrepancy further in Section 4.6.

Fluorescent Fe II $1.6878\ \mu\text{m}$ emission is also thought to originate from a dense circumstellar accretion disc ([Porter et al. 1998](#); [Zorec et al. 2007](#)), in a partially ionized zone between the shielded disc mid-plane and the full ionization zone. However, spectra of massive YSOs exhibiting both fluorescent Fe II and a CO bandhead are rare ([Cooper et al. 2013](#)). The fluorescent Fe II transition at $1.6878\ \mu\text{m}$ occurs when excited atoms/ions (from UV continuum or Lyman series photons) cascade from an upper level of 6.2 eV back down to the ground state. Fe II $1.6878\ \mu\text{m}$ emission lines are detected in both Y544A and Y535A where [Fe II] and Brackett series emission are also prevalent and there is no evidence for H₂ 1–0 S(10) emission. It is possibly present in Y545A. However, this line can also be identified as H₂ 1–0 S(9) and is the more likely identification in this source. It is thought that fluorescent Fe II transition

at $1.6878\ \mu\text{m}$ is more prevalent in massive YSOs ([Lumsden et al. 2012](#)), thus a secure detection in two of our sources corroborates their massive status.

4.6 Comparison of YSOs in the Magellanic Clouds and Galactic high-mass star-forming regions

It is only within the last decade or so that observing large samples of YSO with near-IR spectroscopy is possible outside our own galaxy. Including our sample, 53 K-band spectra of moderate to high resolution have been obtained towards YSOs in the Magellanic Clouds ([Ward et al. 2016, 2017](#); [Rubio et al. 2018](#); [Reiter et al. 2019](#); [van Gelder et al. 2020](#)). These spectra have a diverse range of spectroscopic properties and represent YSOs and unresolved clusters of multiple high-mass stars, across a range of massive YSO evolutionary stages, viewing angles, accretion rates and masses. In Figure 6 we compare the Br γ line luminosities (where available) for these samples and the sample of Galactic high-mass YSOs from [Cooper et al. \(2013\)](#). In all instances there is a very high detection rate of Br γ emission. Given the range of YSO properties the Br γ emission likely originates from several environments including the disc, disc wind and the surrounding low-density ionized gas in H II regions.

Another interesting feature in the K-band is the CO bandhead mentioned earlier, which is seen in emission for massive YSOs and is associated with the dust sublimation region in the inner accretion disc ([Dullemond & Monnier 2010](#); [Ilee et al. 2018](#)). In the Milky Way, the luminosity of the CO bandhead emission correlates with that of Br γ (e.g. [Connelley & Greene 2010](#); [Pomohaci et al. 2017](#)), despite their different kinematic origins ([Hsieh et al. 2021](#)). As noted in Section 4.5, the detection rate of CO bandhead emission in the Magellanic Clouds is extremely low. This raises the intriguing possibility that metallicity substantially affects the physical properties of the accretion disc in massive stars and thus their formation process in metal-poor environments.

In high-mass stars disc accretion remains poorly understood. Here the detection of CO bandhead emission is thought to be dependent on geometry ([Kraus et al. 2000](#); [Barbosa et al. 2003](#)) or accretion rates ([Ilee et al. 2018](#)). Given the diversity of sources and size of both samples, it is unlikely that geometry plays a significant role in the low rate of detection in the Magellanic Clouds. Similarly, unless accretion through the inner gaseous disc occurs by a different mechanism (e.g. episodic versus continuous accretion) or occurs at substantially higher or lower rates compared to Galactic sources (which is not substantiated by the observed Br γ luminosities; see Figure 6) the range of mass accretion rates (and stellar properties of the embedded YSOs that cover the mass range of $5\text{--}30\ M_{\odot}$) appear comparable for both populations and are therefore unlikely to account for the lack of CO bandhead emission.

Dust and gas characteristics depend on the metallicity of the host galaxy. This is a more probable explanation for the low CO bandhead detection rate. In the SMC there is a lower gas-phase CO abundance ([Leroy et al. 2007](#)), higher ambient UV radiation field, and lower dust content compared to solar metallicity gas. Lower CO abundances and reduced shielding from dust allows the intense UV flux to penetrate further into molecular clouds and circumstellar discs. The excitation of the CO bandhead emission requires warm temperatures ($T = 2500\text{--}5000\ \text{K}$) and high densities ($n > 10^{11}\ \text{cm}^{-3}$) so it is thought to trace the inner disc ($r \ll 100\ \text{au}$). Combining the lower CO abundance and the properties of the dust (e.g. [van Loon et al. 2005](#); [Oliveira et al. 2013](#); [Jones et al. 2017](#)) may reduce the likelihood of detecting CO bandhead emission. Less

abundant CO produces fainter emission that is more easily swamped by the continuum. Less dust provides less shielding of CO which may further lower the abundance. Yasui et al. (2010) suggest that lower metallicity discs have a higher ionization fraction which may lead to higher accretion rates, especially if accretion is driven by the magnetorotational instability (although this is not necessarily the case for higher-mass stars, see, e.g. Kuiper et al. 2011).

Tantalisingly, a similar effect is seen in prominent ice bands in the spectra of massive YSOs in the SMC. Oliveira et al. (2011, 2013) found only an upper limit for CO ice. This is most likely caused by a combination of lower gas-phase CO abundance, higher dust temperatures in the SMC YSOs, and the high interstellar radiation field or the cosmic-ray ionization rate affecting gas and grain-surface chemistry (see e.g., Pauly & Garrod 2018). As both gas and ice CO signatures are weak this suggests lower CO abundance overall.

Variations in disc properties (e.g. temperature, density etc.) with metallicity may also affect the CO bandhead emission. For example, in hotter discs not only is the dust-sublimation region larger, but the higher temperatures and gas densities may lead to more of the CO rotational transitions near the bandhead becoming optically thick, further reducing the feature contrast (Ilee et al. 2018). Observations of low-mass stars suggest shorter disc lifetimes in low metallicity regions (Yasui et al. 2009, 2010). If this extends to higher-mass stars as well, stars in the SMC may spend a smaller fraction of their formation time in the narrow range of accretion rates where Ilee et al. (2018) find the CO bandhead is most likely to be detected.

Finally, the spectral resolution of the observations may also influence the detection rate of the first CO overtone, with rates lower for Galactic YSOs observed at high and low resolutions ($R=35000$ – 70000 and $R=500$) versus medium resolution ($R=7000$) data (e.g. Hsieh et al. 2021). Here the relatively weak CO first overtone emission may be masked by the lower SNR or poor contrast above a dusty continuum. The spectral resolving power of the KMOS data is $R\sim 4000$, with other sources in the Magellanic Clouds observed at resolutions between $R=1000$ – 17000 . It is conceivable that, given the distances to the LMC and SMC the CO bandhead remains undetected especially if these sources have a relatively large continuum excess emission. A larger sample with better signal-to-noise ratio and greater spectral resolution is required to conclusively address this issue.

The $1.083\ \mu\text{m}$ feature is one of the brightest He I lines in the IR. As found by Reiter et al. (2019) and Ward et al. (2016, 2017) we also detect He I emission at higher rates ($>40\%$) than seen in high-mass Galactic YSOs; in these local samples the He I $1.083\ \mu\text{m}$ line is detected at a rate of 24% (Pomohaci et al. 2017). Unfortunately, Ward et al. (2016, 2017) did not observe their YSO samples in the Clouds at shorter near-IR wavelengths, and their only detections of He I emission were of the $2.0587\ \mu\text{m}$ line ($2^1P^0-2^5S$) which is outside our spectral range. Nevertheless, our Magellanic Cloud results comparing the He I detection rates appear to be consistently higher than the observed rates for comparable He I lines in the Milky Way (Pomohaci et al. 2017; Cooper et al. 2013). Due to the small sample sizes these trends are tentative, and larger samples of massive-YSOs in both the Magellanic Clouds and the Milky Way are required to confirm any strong correlations with metallicity. We speculate that these differences may arise due to the harder radiation YSOs experienced in the Magellanic Clouds, but the limited number of sources observed at both wavelengths prevents robust statistical analysis of the physical processes that may be responsible for these trends.

5 CONCLUSIONS

We have presented a detailed near-IR spectroscopic study with VLT/KMOS of the NGC 346 star-forming region in the SMC. We targeted massive YSO candidates that were photometrically identified by Sewilo et al. (2013) and Simon et al. (2007) to be in the early stages of formation (Stages I – III; Robitaille et al. 2006). We observed 18 YSO candidates in this region with KMOS, half of which were resolved into multiple objects in the continuum images from the IFUs. From these data we extracted, medium-resolution YJ, H and K band spectra (with $S/N > 10$) for twelve high-mass YSO candidates.

The spectra are rich in features, particularly hydrogen recombination emission lines from the Paschen, Balmer and Pfund series. Nine of the 11 targets with K-band spectroscopy display Br γ emission; H $_2$ and He I are also detected at reasonably high rates ($\sim 45\%$), confirming that these are massive stars in the early phases of formation. No CO bandhead emission is seen in the K-band spectra, which is consistent with previous observations toward young stars in the Small Magellanic Cloud where weak CO bandhead emission has only been detected in one source (Ward et al. 2017). For comparison, the detection rate of the CO first overtone emission is 34% in the Milky Way when observed with similar spectral resolution (Pomohaci et al. 2017). Conversely, the detection of He I $1.083\ \mu\text{m}$ emission is detected at appreciably higher rates in our SMC sample than in the Galaxy. Adding these new detections to other samples in the literature, provides the largest sample of medium-resolution YSO spectroscopy in the Magellanic Clouds, totalling 53 sources, to date. Thus providing better statistical evidence to explore the conditions experienced during the formation of high-mass stars in metal-poor environments compared to the solar neighbourhood.

We have also identified Y533A as an early O-type star and Y548A as slightly cooler star with an early spectral type, from their spectral absorption lines. Radial velocities of the targets are consistent with results for the young population of the SMC. Poor signal-to-noise prevented a detailed exploration of the fainter stars in the KMOS data cubes, with the impact of telluric features also limiting our analysis.

NGC 346 is a target for a Cycle 1 program (Meixner et al. 2017) with the *James Webb Space Telescope* (JWST). With the greater spatial resolution and sensitivity of JWST we will push the study of active star formation in the cluster to solar-mass stars and test our hypothesis that metallicity affects the inner dust sublimation regions of dense accretion discs of massive YSOs, which is traced by the CO first-overtone emission around $2.3\ \mu\text{m}$.

ACKNOWLEDGEMENTS

We would like to thank the referee who’s comments and suggestions significantly improved this paper. OCJ and MR received funding from the EU’s Horizon 2020 program under the Marie Skłodowska-Curie grant agreement No 665593 awarded to the STFC. MR partially supported by an ESO fellowship. This research made use of Astropy,³ a community-developed core Python package for Astronomy (Astropy Collaboration et al. 2013). APLpy, an open-source plotting package for Python (Robitaille & Bressert 2012; Robitaille 2019).

Facilities: VLT.

³ <http://www.astropy.org>

DATA AVAILABILITY

The data underlying this article will be shared on reasonable request to the corresponding author.

REFERENCES

- Astropy Collaboration et al., 2013, *A&A*, **558**, A33
- Barbosa C. L., Damineli A., Blum R. D., Conti P. S., 2003, *AJ*, **126**, 2411
- Bernasconi P. A., Maeder A., 1996, *A&A*, **307**, 829
- Bik A., Kaper L., Waters L. B. F. M., 2006, *A&A*, **455**, 561
- Blum R. D., Ramond T. M., Conti P. S., Figer D. F., Sellgren K., 1997, *AJ*, **113**, 1855
- Blum R. D., Barbosa C. L., Damineli A., Conti P. S., Ridgway S., 2004, *ApJ*, **617**, 1167
- Bolatto A. D., et al., 2007, *ApJ*, **655**, 212
- Bouret J. C., Lanz T., Hillier D. J., Heap S. R., Hubeny I., Lennon D. J., Smith L. J., Evans C. J., 2003, *ApJ*, **595**, 1182
- Bradley L., et al., 2021, astropy/photutils: 1.3.0, doi:10.5281/zenodo.5796924, <https://doi.org/10.5281/zenodo.5796924>
- Calvet N., Muzerolle J., Briceño C., Hernández J., Hartmann L., Saucedo J. L., Gordon K. D., 2004, *AJ*, **128**, 1294
- Calzetti D., Armus L., Bohlin R. C., Kinney A. L., Koornneef J., Storchi-Bergmann T., 2000, *ApJ*, **533**, 682
- Carlson L. R., Sewilo M., Meixner M., Romita K. A., Lawton B., 2012, *A&A*, **542**, A66
- Caulley P. W., Johns-Krull C. M., 2014, *ApJ*, **797**, 112
- Chandler C. J., Carlstrom J. E., Scoville N. Z., 1995, *ApJ*, **446**, 793
- Chen C.-H. R., Chu Y.-H., Gruendl R. A., Gordon K. D., Heitsch F., 2009, *ApJ*, **695**, 511
- Cignoni M., Tosi M., Sabbi E., Nota A., Gallagher J. S., 2011, *AJ*, **141**, 31
- Connelley M. S., Greene T. P., 2010, *AJ*, **140**, 1214
- Connelley M. S., Greene T. P., 2014, *AJ*, **147**, 125
- Connelley M. S., Reipurth B., 2018, *ApJ*, **861**, 145
- Cooper H. D. B., et al., 2013, *MNRAS*, **430**, 1125
- Covey K. R., et al., 2011, *AJ*, **141**, 40
- Cutri R. M., 2MASS Team 2004, in American Astronomical Society Meeting Abstracts. p. 1487
- Dale D. A., et al., 2004, *ApJ*, **601**, 813
- Davies B., Lumsden S. L., Hoare M. G., Oudmaijer R. D., de Wit W.-J., 2010, *MNRAS*, **402**, 1504
- Davies R. I., et al., 2013, *A&A*, **558**, A56
- Davis C. J., et al., 2011, *A&A*, **528**, A3
- De Marchi G., Panagia N., Romaniello M., Sabbi E., Sirianni M., Prada Moroni P. G., Degl'Innocenti S., 2011, *ApJ*, **740**, 11
- Dimaratos A., Cormier D., Bigiel F., Madden S. C., 2015, *A&A*, **580**, A135
- Drew J. E., Bunn J. C., Hoare M. G., 1993, *MNRAS*, **265**, 12
- Dufton P. L., Evans C. J., Hunter I., Lennon D. J., Schneider F. R. N., 2019, *A&A*, **626**, A50
- Dufton P. L., Evans C. J., Lennon D. J., Hunter I., 2020, *A&A*, **634**, A6
- Dullemond C. P., Monnier J. D., 2010, *ARA&A*, **48**, 205
- Earl N., et al., 2022, astropy/specutils: V1.7.0, doi:10.5281/zenodo.6207491, <https://doi.org/10.5281/zenodo.6207491>
- Edwards S., Fischer W., Hillenbrand L., Kwan J., 2006, *ApJ*, **646**, 319
- Evans C. J., Howarth I. D., 2008, *MNRAS*, **386**, 826
- Evans C. J., Lennon D. J., Smartt S. J., Trundle C., 2006, *A&A*, **456**, 623
- Fischer W., Kwan J., Edwards S., Hillenbrand L., 2008, *ApJ*, **687**, 1117
- Freudling W., Romaniello M., Bramich D. M., Ballester P., Forchi V., García-Dabó C. E., Moehler S., Neeser M. J., 2013, *A&A*, **559**, A96
- Giannini T., et al., 2013, *ApJ*, **778**, 71
- Gordon K. D., Clayton G. C., Misselt K. A., Landolt A. U., Wolff M. J., 2003, *ApJ*, **594**, 279
- Gordon K. D., et al., 2011, *AJ*, **142**, 102
- Hanson M. M., Kudritzki R. P., Kenworthy M. A., Puls J., Tokunaga A. T., 2005, *ApJS*, **161**, 154
- Harris J., Zaritsky D., 2006, *AJ*, **131**, 2514
- Henize K. G., 1956, *ApJS*, **2**, 315
- Hennekemper E., Gouliermis D. A., Henning T., Brandner W., Dolphin A. E., 2008, *ApJ*, **672**, 914
- Hsieh T.-H., et al., 2021, *ApJ*, **912**, 108
- Hutsemekers D., 1994, *A&A*, **281**, L81
- Ilee J. D., et al., 2013, *MNRAS*, **429**, 2960
- Ilee J. D., Oudmaijer R. D., Wheelwright H. E., Pomohaci R., 2018, *MNRAS*, **477**, 3360
- Jones O. C., et al., 2017, *MNRAS*, **470**, 3250
- Kato D., et al., 2007, *PASJ*, **59**, 615
- Kausch W., et al., 2015, *A&A*, **576**, A78
- Keller S. C., Wood P. R., Bessell M. S., 1999, *A&AS*, **134**, 489
- Kennicutt R. C. J., 1984, *ApJ*, **287**, 116
- Kraemer K. E., Sloan G. C., Wood P. R., Jones O. C., Egan M. P., 2017, *ApJ*, **834**, 185
- Kraus M., Krügel E., Thum C., Geballe T. R., 2000, *A&A*, **362**, 158
- Kudritzki R. P., 2002, *ApJ*, **577**, 389
- Kuiper R., Klahr H., Beuther H., Henning T., 2011, *ApJ*, **732**, 20
- Lacy J. H., Sneden C., Kim H., Jaffe D. T., 2017, *ApJ*, **838**, 66
- Lee Y.-H., Koo B.-C., Lee J.-J., Burton M. G., Ryder S., 2019, *AJ*, **157**, 123
- Leroy A., Bolatto A., Stanimirovic S., Mizuno N., Israel F., Bot C., 2007, *ApJ*, **658**, 1027
- Lumsden S. L., Wheelwright H. E., Hoare M. G., Oudmaijer R. D., Drew J. E., 2012, *MNRAS*, **424**, 1088
- Martayan C., Baade D., Fabregat J., 2010, *A&A*, **509**, A11
- Massey P., Parker J. W., Garmany C. D., 1989, *AJ*, **98**, 1305
- Meixner M., et al., 2017, NGC 346: Star Formation at Low Metallicity in the Small Magellanic Cloud, JWST Proposal. Cycle 1
- Mendigutía I., Calvet N., Montesinos B., Mora A., Muzerolle J., Eiroa C., Oudmaijer R. D., Merín B., 2011, *A&A*, **535**, A99
- Momcheva I. G., Lee J. C., Ly C., Salim S., Dale D. A., Ouchi M., Finn R., Ono Y., 2013, *AJ*, **145**, 47
- Mouri H., Kawara K., Taniguchi Y., 2000, *ApJ*, **528**, 186
- Nazé Y., Hartwell J. M., Stevens I. R., Corcoran M. F., Chu Y. H., Koenigsberger G., Moffat A. F. J., Niemela V. S., 2002, *ApJ*, **580**, 225
- Nota A., et al., 2006, *ApJL*, **640**, L29
- Ochsendorf B. B., Zinnecker H., Nayak O., Bally J., Meixner M., Jones O. C., Indebetouw R., Rahman M., 2017, *Nature Astronomy*, **1**, 784
- Oliveira J. M., et al., 2011, *MNRAS*, **411**, L36
- Oliveira J. M., et al., 2013, *MNRAS*, **428**, 3001
- Oliveira J. M., et al., 2019, *MNRAS*, **490**, 3909
- Pauly T., Garrod R. T., 2018, *ApJ*, **854**, 13
- Peimbert M., Peimbert A., Ruiz M. T., 2000, *ApJ*, **541**, 688
- Pomohaci R., Oudmaijer R. D., Lumsden S. L., Hoare M. G., Mendigutía I., 2017, *MNRAS*, **472**, 3624
- Porter J. M., Drew J. E., Lumsden S. L., 1998, *A&A*, **332**, 999
- Reiter M., et al., 2018, *ApJ*, **852**, 5
- Reiter M., Nayak O., Meixner M., Jones O., 2019, *MNRAS*, **483**, 5211
- Robitaille T., 2019, APLpy v2.0: The Astronomical Plotting Library in Python, doi:10.5281/zenodo.2567476, <https://doi.org/10.5281/zenodo.2567476>
- Robitaille T., Bressert E., 2012, APLpy: Astronomical Plotting Library in Python, Astrophysics Source Code Library (ascl:1208.017)
- Robitaille T. P., Whitney B. A., Indebetouw R., Wood K., Denzmore P., 2006, *ApJS*, **167**, 256
- Robitaille T., Ginsburg A., Beaumont C., Leroy A., Rosolowsky E., 2016, spectral-cube: Read and analyze astrophysical spectral data cubes (ascl:1609.017)
- Rousselot P., Lidman C., Cuby J. G., Moreels G., Monnet G., 2000, *A&A*, **354**, 1134
- Rubio M., Barbá R. H., Kalari V. M., 2018, *A&A*, **615**, A121
- Ruffle P. M. E., et al., 2015, *MNRAS*, **451**, 3504
- Sabbi E., et al., 2007, *AJ*, **133**, 44
- Seale J. P., et al., 2014, *AJ*, **148**, 124
- Sewilo M., et al., 2013, *ApJ*, **778**, 15
- Sewilo M., et al., 2022, arXiv e-prints, p. arXiv:2201.09945
- Sharples R., et al., 2013, The Messenger, **151**, 21
- Simon J. D., et al., 2007, *ApJ*, **669**, 327

- Skrutskie M. F., et al., 2006, *AJ*, **131**, 1163
 Smette A., et al., 2015, *A&A*, **576**, A77
 Stanimirovic S., Staveley-Smith L., Dickey J. M., Sault R. J., Snowden S. L., 1999, *MNRAS*, **302**, 417
 Stetson P. B., 1987, *PASP*, **99**, 191
 Storey P. J., Hummer D. G., 1995, *MNRAS*, **272**, 41
 Udalski A., Szymanski M. K., Soszynski I., Poleski R., 2008, *Acta Astron.*, **58**, 69
 Ward J. L., Oliveira J. M., van Loon J. T., Sewilo M., 2016, *MNRAS*, **455**, 2345
 Ward J. L., Oliveira J. M., van Loon J. T., Sewilo M., 2017, *MNRAS*, **464**, 1512
 Wegner M., Muschielok B., 2008, in *Proc. SPIE.* p. 70190T, doi:10.1117/12.787190
 Whelan D. G., Leboutteiller V., Galliano F., Peeters E., Bernard-Salas J., Johnson K. E., Indebetouw R., Brandl B. R., 2013, *ApJ*, **771**, 16
 Wilke K., Klaas U., Lemke D., Mattila K., Stickel M., Haas M., 2004, *A&A*, **414**, 69
 Woods P. M., et al., 2011, *MNRAS*, **411**, 1597
 Yasui C., Kobayashi N., Tokunaga A. T., Saito M., Tokoku C., 2009, *ApJ*, **705**, 54
 Yasui C., Kobayashi N., Tokunaga A. T., Saito M., Tokoku C., 2010, *ApJL*, **723**, L113
 Yeh S. C. C., Seauquist E. R., Matzner C. D., Pellegrini E. W., 2015, *ApJ*, **807**, 117
 Zaritsky D., Harris J., Thompson I. B., Grebel E. K., Massey P., 2002, *AJ*, **123**, 855
 Zorec J., Arias M. L., Cidale L., Ringuet A. E., 2007, *A&A*, **470**, 239
 de Grijs R., Bono G., 2015, *AJ*, **149**, 179
 van Gelder M. L., et al., 2020, *A&A*, **636**, A54
 van Loon J. T., Marshall J. R., Zijlstra A. A., 2005, *A&A*, **442**, 597

APPENDIX A: CONTINUUM IMAGES

The continuum maps were generated using the *SPECTRALCUBE* (Robitaille et al. 2016) python package and displayed with *APLPY* using a linear stretch, autoscaled to the peak flux. In the 2MASS 6x catalogue (Cutri & 2MASS Team 2004) seven of the 18 original YSO candidates in our sample have matches to multiple sources within 1", thus the detection of multiples in the KMOS data cubes is expected. The RA and Dec. positions of each source resolved and automatically detected using *DAOSTARFINDER* in *PHOTUTILS* ($>5\sigma$ detection above the background in the continuum flux maps) are given in Table 2, sources $>3\sigma$ are listed in Table A1. In instances where multiple sources were present, the brightest source in the cube was identified with an 'A' suffix, with fainter sources designated 'B' and 'C'. No cube had more than two sources with fluxes $>5\sigma$ above the background. Potential sources with $<5\sigma$ detections are not considered further.

APPENDIX B: EMISSION LINE FLUXES

Table B1 provides summary of all detected spectral features for each object our NGC 346 KMOS sample, together with their measured emission-line fluxes. The measurement of the line fluxes is described in Section 3.2.2. A question mark (?) indicates that the line identification is uncertain. The fluxes have not been corrected for extinction. We do not provide line measurements for Pfund series emission and other lines (tentatively) identified in this region of the spectrum due to the increased noise from atmospheric transmission. Similarly, if the line is present but in absorption an "A" is listed instead of a flux.

Table A1. List of all sources with a $>3\sigma$ detection as determined by *DAOSTARFINDER* present in our KMOS datacubes. The wavelengths at which the source was detected is denoted by a check mark.

ID	RA [J2000]	Dec [J2000]	S/N >3 Detection		
			YJ	H	K
Y519A	00h58m40.240s	-72d11m22.19s	✓
Y523A	00h58m49.401s	-72d12m55.12s	✓
Y524A	00h58m53.567s	-72d12m54.78s	✓	✓	...
Y525A	00h58m55.641s	-72d08m31.99s	✓	✓	✓
Y525B	00h58m55.357s	-72d08m31.67s	✓	✓	...
Y525C	00h58m55.902s	-72d08m31.23s	...	✓	...
Y528A	00h58m57.148s	-72d12m35.36s	✓	✓	✓
Y528B	00h58m56.809s	-72d12m34.85s	✓	✓	...
Y532A	00h59m02.536s	-72d10m07.60s	✓	✓	✓
Y533A	00h59m02.923s	-72d10m34.90s	✓	✓	✓
Y535A	00h59m05.304s	-72d10m35.50s	✓	✓	✓
Y535B	00h59m05.664s	-72d10m35.04s	✓
Y538A	00h59m08.550s	-72d11m03.13s	✓	✓	✓
Y538B	00h59m08.833s	-72d11m03.66s	✓	✓	...
Y543A	00h59m11.654s	-72d12m23.74s	✓	✓	✓
Y544A	00h59m12.250s	-72d09m58.56s	✓	✓	✓
Y544B	00h59m12.333s	-72d10m00.25s	✓	✓	✓
Y545A	00h59m14.122s	-72d09m28.47s	✓	✓	✓
Y545B	00h59m14.230s	-72d09m26.88s	✓	✓	...
Y545C	00h59m13.828s	-72d09m27.70s	...	✓	...
Y547A	00h59m14.988s	-72d11m02.31s	✓	✓	✓
Y548A	00h59m17.046s	-72d09m14.86s	✓	✓	✓
Y549A	00h59m17.141s	-72d11m23.88s	✓	✓	✓
Y551A	00h59m19.209s	-72d09m30.29s	✓	✓	✓
Y551B	00h59m18.951s	-72d09m30.29s	✓	✓	...
Y553A	00h59m20.660s	-72d11m20.83s	✓	✓	✓
Y553B	00h59m20.421s	-72d11m22.19s	✓
Y556A	00h59m23.754s	-72d12m56.32s	✓	✓	✓
Y556B	00h59m23.953s	-72d12m55.12s	✓	✓	...
Y556C	00h59m23.702s	-72d12m54.78s	✓	✓	...

Table B1. Common emission line fluxes towards the resolved-point sources in our NGC 346 KMOS sample, subdivided into the JY, H and K wavelength bands by the horizontal lines. Fluxes are given in W m^{-2} . "P" denotes that a line is present but a reliable estimate of its line flux is not possible due to the low contrast above (or poor fit to) the local continuum. "A" indicates that a line is present but is in absorption. The fluxes have not been corrected for extinction. Where a spectra was not obtained '–' is marked in the table. A ':' indicates that the line may have a potential P Cygni profile.

Source ID Line	525A (Wm^{-2})	532A (Wm^{-2})	533A (Wm^{-2})	535A (Wm^{-2})	538A (Wm^{-2})	544A (Wm^{-2})	544B (Wm^{-2})	545A (Wm^{-2})	548A (Wm^{-2})	549A (Wm^{-2})	553A (Wm^{-2})	556A (Wm^{-2})
He I	$<1.7 \times 10^{-19}$	$2.08 \pm 0.12 \times 10^{-19}$	A	$1.46 \pm 0.07 \times 10^{-18}$	–	$1.51 \pm 0.07 \times 10^{-18}$	–	$2.68 \pm 0.25 \times 10^{-20}$	A	–	$<6.3 \times 10^{-19}$	$<9.9 \times 10^{-20}$
Paschen 6-3	$<6.1 \times 10^{-20}$	$3.26 \pm 0.13 \times 10^{-19}$	A	$7.55 \pm 0.17 \times 10^{-18}$	–	$5.33 \pm 0.13 \times 10^{-18}$	–	$6.83 \pm 0.20 \times 10^{-19}$	$<5.9 \times 10^{-21}$	–	$5.78 \pm 0.21 \times 10^{-20}$	$6.95 \pm 0.22 \times 10^{-19}$
[Fe II]	$<2.3 \times 10^{-20}$	$<1.9 \times 10^{-20}$	$<9.3 \times 10^{-20}$	$7.25 \pm 0.64 \times 10^{-19}$	–	$1.67 \pm 0.24 \times 10^{-19}$	–	$5.56 \pm 1.30 \times 10^{-20}$	$<3.1 \times 10^{-20}$	–	$6.00 \pm 1.00 \times 10^{-20}$	$<3.8 \times 10^{-20}$
Paschen 5-3	A?	$6.84 \pm 0.21 \times 10^{-19}$	A	$1.47 \pm 0.03 \times 10^{-17}$	–	$8.46 \pm 0.23 \times 10^{-18}$	–	$1.40 \pm 0.02 \times 10^{-18}$	A	–	$1.47 \pm 0.05 \times 10^{-18}$	$1.28 \pm 0.04 \times 10^{-18}$
Brackett 12-4	–	$<7.6 \times 10^{-18}$ P	$<1.1 \times 10^{-20}$	$1.05 \pm 0.07 \times 10^{-18}$	–	$4.67 \pm 0.14 \times 10^{-19}$	–	$<8.5 \times 10^{-21}$	–	–	–	$8.98 \pm 1.03 \times 10^{-20}$
Brackett 11-4	–	$<7.1 \times 10^{-18}$ P	A	$1.27 \pm 0.10 \times 10^{-18}$	–	$5.40 \pm 0.20 \times 10^{-19}$	–	$<9.1 \times 10^{-21}$	–	–	–	$9.95 \pm 0.55 \times 10^{-20}$
H ₂ 1-0 S(9)/Fe II	–	A	A	$2.99 \pm 0.45 \times 10^{-19}$	–	$1.37 \pm 0.16 \times 10^{-19}$	–	$1.79 \pm 0.08 \times 10^{-19}$	–	–	–	$<3.5 \times 10^{-20}$
Brackett 10-4	–	$<3.4 \times 10^{-18}$ P	A	$1.39 \pm 0.11 \times 10^{-18}$	–	$6.94 \pm 0.23 \times 10^{-19}$	–	$<7.5 \times 10^{-20}$ P	–	–	–	$1.16 \pm 0.07 \times 10^{-19}$
H ₂ 1-0:S(1)	–	$5.07 \pm 0.60 \times 10^{-19}$	A	$1.36 \pm 0.25 \times 10^{-18}$	$1.39 \pm 0.24 \times 10^{-19}$	$4.13 \pm 0.76 \times 10^{-19}$	$3.29 \pm 0.31 \times 10^{-19}$	$<3.5 \times 10^{-20}$	$<2.8 \times 10^{-20}$	$4.07 \pm 0.39 \times 10^{-19}$	$<4.4 \times 10^{-20}$	$1.08 \pm 0.06 \times 10^{-19}$
Brackett 7-4	–	$3.35 \pm 0.54 \times 10^{-19}$	$<9.6 \times 10^{-21}$	$4.46 \pm 0.16 \times 10^{-18}$	$<6.7 \times 10^{-20}$ P	$2.04 \pm 0.18 \times 10^{-18}$	$1.82 \pm 0.18 \times 10^{-19}$	$2.50 \pm 0.11 \times 10^{-19}$	$<4.8 \times 10^{-20}$	$5.20 \pm 0.40 \times 10^{-19}$	$4.36 \pm 0.14 \times 10^{-19}$	$2.92 \pm 0.05 \times 10^{-19}$
H ₂ 1-0 S(0)	–	$1.47 \pm 0.61 \times 10^{-19}$	$<3.1 \times 10^{-20}$	$<4.7 \times 10^{-19}$	$<4.7 \times 10^{-20}$	$1.56 \pm 0.81 \times 10^{-19}$	$5.78 \pm 1.20 \times 10^{-20}$	$<1.7 \times 10^{-20}$	$7.00 \pm 4.01 \times 10^{-20}$	$1.46 \pm 0.20 \times 10^{-19}$	$<5.4 \times 10^{-20}$	$<6.5 \times 10^{-20}$

This paper has been typeset from a \LaTeX file prepared by the author.